JACS
JOURNAL OF THE AMERICAN CHEMICAL SOCIETY
pubs.acs.org/JACS
Article

Enzymatically Forming Intranuclear Peptide Assemblies for Selectively Killing Human Induced Pluripotent Stem Cells

Shuang Liu, Qiuxin Zhang, Adrianna N. Shy, Meihui Yi, Hongjian He, Shijiang Lu, and Bing Xu*

Cite This: J. Am. Chem. Soc. 2021, 143, 15852−15862
Read Online
ACCESS | Metrics & More | Article Recommendations | Supporting Information

ABSTRACT: Tumorigenic risk of undifferentiated human induced pluripotent stem cells (iPSCs), being a major obstacle for clinical application of iPSCs, requires novel approaches for selectively eliminating undifferentiated iPSCs. Here, we show that an L-phosphopentapeptide, upon the dephosphorylation catalyzed by alkaline phosphatase (ALP) overexpressed by iPSCs, rapidly forms intranuclear peptide assemblies made of α-helices to selectively kill iPSCs. The phosphopentapeptide, consisting of four L-leucine residues and a C-terminal L-phosphotyrosine, self-assembles to form micelles/nanoparticles, which transform into peptide nanofibers/nanoribbons after enzymatic dephosphorylation removes the phosphate group from the L-phosphotyrosine. The concentration of ALP and incubation time dictates the morphology of the peptide assemblies. Circular dichroism and FTIR indicate that the L-pentapeptide in the assemblies contains a mixture of an α-helix and aggregated strands. Incubating the L-phosphopentapeptide with human iPSCs results in rapid killing of the iPSCs (=<2 h) due to the significant accumulation of the peptide assemblies in the nuclei of iPSCs. The phosphopentapeptide is innocuous to normal cells (e.g., HEK293 and hematopoietic progenitor cell (HPC)) because normal cells hardly overexpress ALP. Inhibiting ALP, mutating the L-phosphotyrosine from the C-terminal to the middle of the phosphopentapeptides, or replacing L-leucine to D-leucine in the phosphopentapeptide abolishes the intranuclear assemblies of the pentapeptides. Treating the L-phosphopentapeptide with cell lysate of normal cells (e.g., HS-5) confirms the proteolysis of the L-pentapeptide. This work, as the first case of intranuclear assemblies of peptides, not only illustrates the application of enzymatic noncovalent synthesis for selectively targeting nuclei of cells but also may lead to a new way to eliminate other pathological cells that express a high level of certain enzymes.

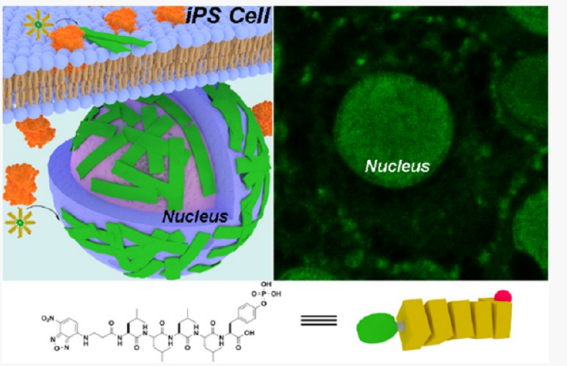

INTRODUCTION

Having the unprecedented potential to generate a variety of cell types for cell therapy, pluripotent stem cells (PSCs), such as human embryonic stem cells (ESC) and human induced pluripotent stem cells (iPSCs), promise to revolutionize personalized medicine.[1] Increased research efforts have focused on the use of PSCs in clinical applications, such as PSC-derived dopamine (DA) neurons for treating Parkinson's disease,[2] differentiating PSC into cardiomyocytes[3] or epicardium cells[4] for treating heart disease, the generation of insulin-producing pancreatic beta cells from PSCs for treating diabetes,[5] photoreceptor progenitors derived from PSCs for treating blindness,[6] and PSC-derived retinal pigment epithelium (RPE) for treating age-related macular degeneration (AMD).[7] Despite the rapid progress of iPSC technology, considerable challenges remain to be met before safe clinical applications of PSCs.[8,9] Because a key feature of iPSCs is their potential for infinite proliferation, one major safety concern of iPSCs is their tumorigenicity.[10] For example, undifferentiated iPSCs exhibit comparable tumor producing potential with that of HeLa cells in a rat model.[11] Several studies even have shown a small number of residual iPSCs may produce teratomas in animals.[12,13] Moreover, inefficient differentiation protocols, variability of differentiation efficiency, or heterogeneity of iPSC clones all can lead to residual or large numbers of undifferentiated iPSCs after the differentiation procedure.[14] Thus, it is necessary to eliminate the undifferentiated iPSCs without harming differentiated cells in a cell mixture prior to cell transplantation. Considerable efforts have been spent on developing approaches to eliminate residual undifferentiated iPSCs[15−36] for the safe clinical applications of iPSC-based cell therapy, but current strategies still have many drawbacks. Therefore, it is still necessary to develop an innovative strategy that is rapid (=< 2 h), effective, and general for eliminating undifferentiated iPSCs in cell mixtures.

A prominent difference between iPSCs and differentiated cells is that iPSCs overexpress (or upregulate) alkaline phosphatase (ALP),[37] but the differentiated cells do not.

Received: August 3, 2021
Published: September 16, 2021

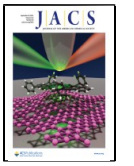

Thus, it is possible to selectively kill iPSCs by using enzyme-instructed self-assembly (EISA),[38−49] a molecular process that integrates enzyme reactions and self-assembly and is known to selectively kill cells based on overexpression of enzymes.[46,50−52] In fact, Saito et al. recently reported selectively eliminating iPSCs by EISA of D-phosphotetrapeptides.[53] Taking the advantage that ALP acts as an ectophosphatase to form pericellular nanofibers of D-peptides,[51] they have shown that ALP overexpressed on iPSCs dephosphorylates the D-phosphotetrapeptides (e.g., **1**) into hydrophobic peptides, which self-assemble on the cell surface to induce cell death. They demonstrated that 2 h of the D-phosphopeptide treatment eliminates iPSCs and prevents residual iPSC-induced teratoma formation in a mouse tumorigenicity assay.[53] Although that work confirms EISA as a feasible approach for selectively and rapidly eliminating residual iPSCs, there are still drawbacks: (i) The D-phosphotetrapeptide undergoes pericellular EISA,[53] thus it is unable to utilize intracellular ALP.[54] (ii) The D-peptides, being proteolytic resistant, self-assemble to form β-sheets, which is considered to be amyloidogenic.[55,56]

Here, we show that an L-phosphopentapeptide (**5**), upon the dephosphorylation catalyzed by ALP, rapidly forms intranuclear peptide assemblies made of an α-helix and aggregated strands to selectively kill iPSCs (Figure 1). Specifically, the phosphopentapeptide, consisting of four L-leucine residues and a C-terminal L-phosphotyrosine, self-assembles to form micelles or nanoparticles, which transform into peptide nanofibers or nanoribbons after enzymatic dephosphorylation removes the phosphate group from the phosphotyrosine. The concentrations of ALP dictate the morphology of the pentapeptide assemblies. While a high expression level of ALP (800 U/L) catalyzes the dephosphorylation of the L-phosphopentapeptide to form nanoribbons, a normal expression level of ALP (100 U/L) for the dephosphorylation results in nanofibers, depending on the time of incubation. Circular dichroism indicates that the L-pentapeptide adopts an α-helix and aggregated strand. Incubating the phosphopentapeptide with human iPSCs results in rapid killing of the iPSCs (=< 2 h) due to the accumulation of the pentapeptide assemblies in the iPSC nuclei. The phosphopentapeptide is innocuous to normal cells (e.g., HEK293 and hematopoietic progenitor cell (HPC)). Inhibiting ALP abolishes the intranuclear assemblies. Mutating the L-phosphotyrosine from the C-terminal to the middle of the phosphopentapeptides or replacing L-leucine to D-leucine generates the phosphopentapeptides that undergo enzymatic self-assembly to form thin nanofibers. These two phosphopentapeptides are unable to result in intranuclear peptide assemblies for killing iPSCs. Treating the L-phosphopentapeptide with cell lysates of normal cells (e.g., HS-5) confirms the proteolysis of the L-pentapeptides. Compared to the previous approach,[53] there are several significant advancements: (i) the L-phosphopeptides enter cells to undergo EISA to form intranuclear peptide assemblies. (ii) L-Peptide nanoribbons made of peptide α-helices minimize the risk of amyloidogenicity due to β-sheets. (iii) After killing the iPSCs, the L-peptides undergo proteolysis to form L-amino acids, thus minimizing side effects. This work, as the first case of intranuclear assemblies of peptides, illustrates the application of enzymatic noncovalent synthesis[57] for selectively targeting nuclei of cells.

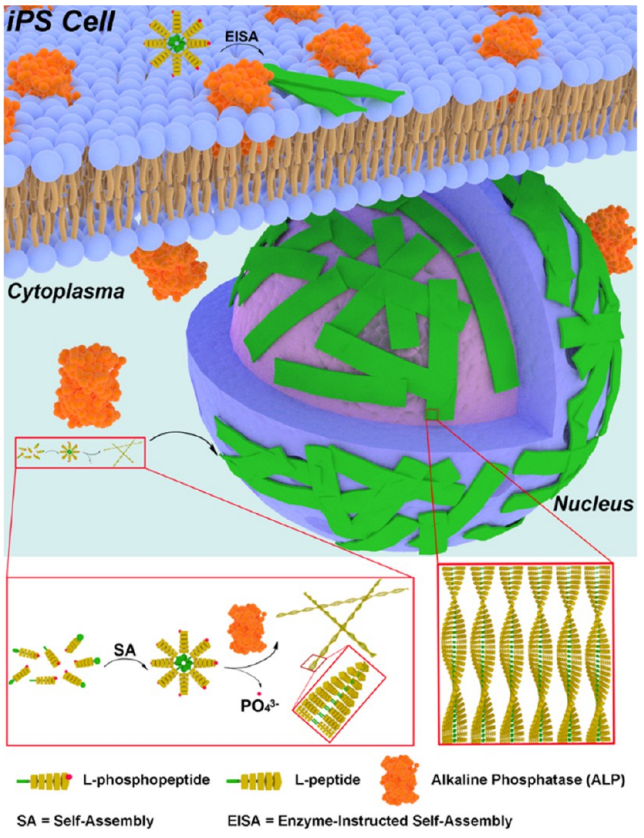

Figure 1. Schematic representation of EISA of L-phosphopentapeptide (**5**) to result in intranuclear assemblies of **6**.

RESULTS AND DISCUSSION

Molecular Design and Synthesis. In the previously reported study,[53] the substrate for EISA is a D-phosphotetrapeptide (**1**, Figure 2A), consisting of a 2-naphthylacetyl group to enhance $\pi-\pi$ interactions, a D-Phe-D-Phe-D-Phe as the β-sheet forming motif, and a D-phosphotyrosine as the trigger for ALP-catalyzed dephosphorylation. After enzymatic dephosphorylation, **1** becomes **2**. The self-assembly of **2** forms β-sheets.[53] Occurring on iPSCs, such a molecular process selectively kills iPSCs.[53] To minimize the formation of β-sheets and to maintain the hydrophobicity for self-assembly in water, we decide to use L-leucine (Leu) as the amino acid for constructing the peptide backbone because leucine is known to have high helix propensity.[58] To visualize the location of the peptide assemblies in a cellular environment after EISA, we replace the 2-naphthylacetyl group with NBD (4-nitro-2,1,3-benzoxadiazole, an environment-sensitive fluorophore) that is particularly useful for revealing peptide assemblies in cells.[59,60]

Following the above rationale, we design the phosphopeptide NBD-LLL_pY (**3**). Although **3** is able to turn into **4** upon dephosphorylation catalyzed by ALP, **4** only exhibits limited self-assembling ability (Figures S11 and S12). Thus, we increase the number of leucine in **3** to make NBD-$LLLL_pY$ (**5**, Figure 2B). For further understanding the self-assembly of this leucine-rich sequence, we also design two other phosphopentapeptides, **7** and **9**. We move L-phosphotyrosine from the C-terminal to the middle of **5** to give NBD-LL_pYLL (**7**). By placing tyrosine between two dileucine motifs, we expect **8**, the corresponding pentapeptide of **7**, would be less prone for α-helix conformation because tyrosine is less prone to form a helix than leucine.[61] In another analog, we keep L-

https://doi.org/10.1021/jacs.1c07923
J. Am. Chem. Soc. 2021, 143, 15852−15862

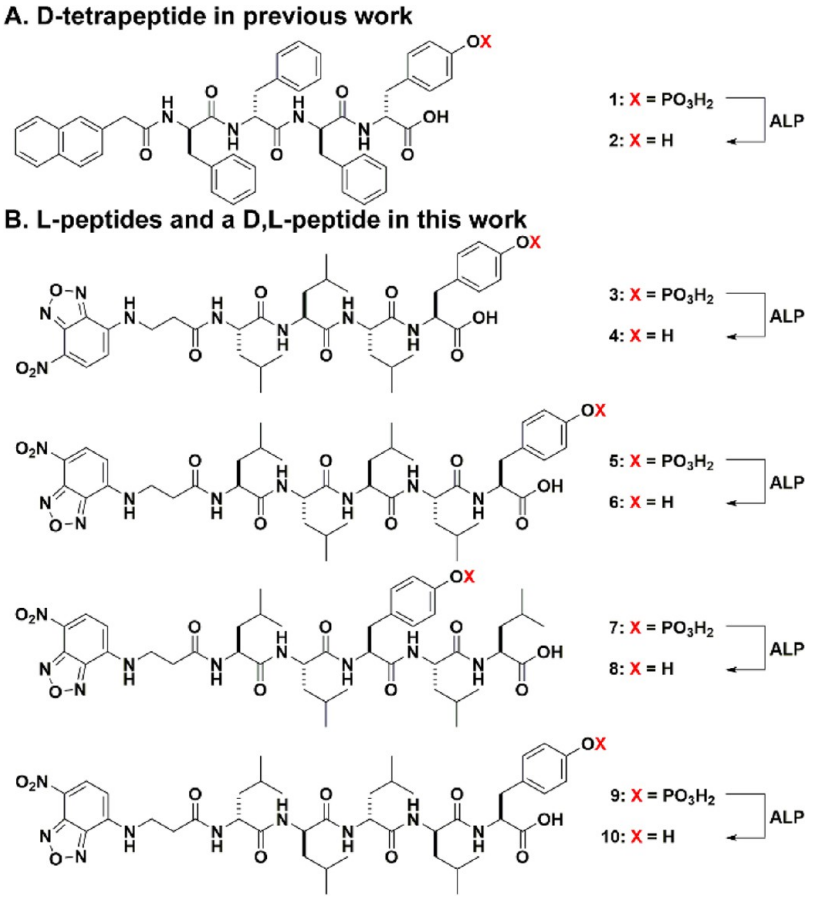

Figure 2. (A) Chemical structure of D-tetrapeptide in previous work.[53] (B) Chemical structures of L-peptides and a D,L-peptide in this work.

phosphotyrosine but replace the L-Leu in **5** by D-Leu. Such a change results in NBD-llll$_p$Y (**9**, l represents D-Leu). **9** and its corresponding pentapeptide (**10**) are heterochiral peptides, which would help understand the effect of homochirality contributing to the morphology of the peptide assemblies. Based on the molecular design shown in Figure 2B, we use solid phase peptide synthesis (SPPS) to make the phosphopeptides (**5**, **7**, and **9**; Scheme S1). Briefly, after the reaction between NBD-Cl and β-alanine to produce NBD-β-alanine[62] and protecting L-phosphotyrosine by 9-fluorenylmethoxycarbonyl (Fmoc), the designed precursors are synthesized via SPPS by using Fmoc-protected amino acids. After purification by high performance liquid chromatography (HPLC), all the precursors are confirmed by LC-MS and ^{1}H NMR (Figures S1−S10).

Enzymatic Self-Assembly in PBS. After obtaining all the precursors via SPPS, we evaluate their behaviors for EISA in vitro by using transmission electron microscopes (TEMs) to examine the nanostructures formed before and after the ALP-catalyzed dephosphorylation of precursors, **5**, **7**, and **9**. At 400 μM and in phosphate buffered saline (PBS), **5** self-assembles to form short nanofibers with the diameter of 9 ± 2 nm and a few nanoparticles (Figure 3). The critical micelle concentration (CMC) of **5** is 86.1 μM (Figure S13A). In the solution of **7** (400 μM) and **9** (400 μM), TEM images show nanoparticles only, and the CMCs of **7** and **9** are 159.9 μM and 146.8 μM, respectively (Figure S13C,E). These results indicate that, among the three phosphopentapeptides, **5** exhibits a higher self-assembling ability than **7** or **9** does. After the solution of **5** (400 μM) being incubated with ALP (0.5 U/mL) at 37 °C for 24 h, TEM shows that dephosphorylation of **5** results in nanoribbons with the widths of 74 ± 13 nm. Figure S15 shows the folded nanoribbons, indicating the self-assembly nanostructures are more like nanoribbons than nanotubes. Moreover, the lack of features of nanotubes, such as circular cross profiles, double layer of tubes, and the broken ends, in the TEM images suggests that the morphology of the assemblies of **6** likely is curved nanoribbons. The CMC of **6** is 8.1 μM (Figure S13B). Unlike the case of **5**, dephosphorylation of **7** or **9** at 400 μM by ALP (0.5 U/mL) produces nanofibers with the diameters of 6 ± 2 nm or 9 ± 2 nm, whose CMC is 87.4 μM or 25.8 μM (Figure S13D,F), respectively.

A key requirement for selectively eliminating iPSCs by EISA is that the L-peptide nanoribbons only form on and in iPSCs, which overexpress ALP, but not on and in the differentiated cells that express a normal level of ALP. That is, L-peptide nanoribbons should only rapidly form at a high level of ALP but not at a normal level of ALP. Considering that the normal level of ALP in serum is about 0.1 U/mL[63] and an abnormally high level of ALP can be 0.6−0.8 U/mL,[64,65] we test EISA of **5** in the presence of different concentrations of ALP (from 0.1 U/mL to 0.8 U/mL) for 1 and 2 h (Figure 4). We choose to focus on **5** because it selectively kills iPSCs (*vide infra*). One hour after the addition of ALP in the solution of **5** (400 μM), TEM shows that nanofibers form in the presence of 0.1 U/mL ALP, and the mixture of nanofibers and nanoribbons forms at 0.2 and 0.4 U/mL ALP, with more nanofibers at 0.2 U/mL ALP and more nanoribbons at 0.4 U/mL ALP. When the concentrations of ALP are at 0.6 and 0.8 U/mL, TEM shows dominantly nanoribbons. After 2 h of incubation of the

https://doi.org/10.1021/jacs.1c07923
J. Am. Chem. Soc. 2021, 143, 15852−15862

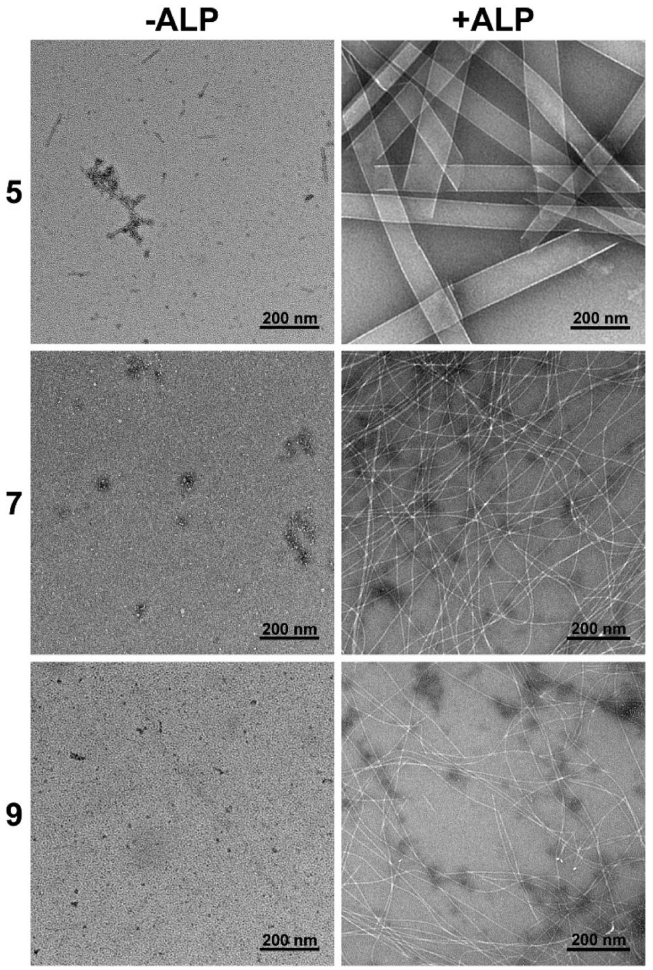

Figure 3. Transmission electron microscopy (TEM) imaging of **5**, **7**, and **9** (400 μM, PBS) and the corresponding **6**, **8**, and **10** formed by adding ALP (0.5 U/mL) for 24 h.

solution of **5** (400 μM) with ALP, TEM shows that dephosphorylation of **5** results in nanoribbons when the concentrations of ALP are 0.1, 0.2, 0.4, 0.6, and 0.8 U/mL. Notably, by decreasing the concentration of **5** to 200 μM, a 1 h treatment by 0.1 U/mL or 0.8 U/mL ALP results in nanoparticles with the diameters of 404 ± 50 nm or the nanoribbons (Figure S14), respectively. These results indicate that the initial concentration of **5**, the expression levels of ALP, and the time of dephosphorylation control morphology of the nanoscale assemblies of the L-pentapeptides formed by EISA, similar to the case that the ratio of substrates and enzymes controls the rheological properties of hydrogels made by EISA.[66] This feature is essential for using EISA to target cells selectively.

Enzymatic Conversion. The morphological differences shown in Figures 3 and 4 imply that the extent of enzymatic reactions likely controls the self-assembly. Thus, we examine the conversion of the phosphopentapeptides to their corresponding peptides over time. We incubate **5**, **7**, or **9** at the concentration of 100, 200, or 400 μM with 0.5 U/mL ALP and measure their dephosphorylation ratio at different time points (Figure 5). We choose the concentration of ALP to be 0.5 U/mL because iPSCs overexpress ALP[37] and nanoribbons of **5** formed within 1 h when the ALP is >0.4 U/mL (Figure 4). Figure 5A shows the half-lives of **5** at 100, 200, and 400 μM

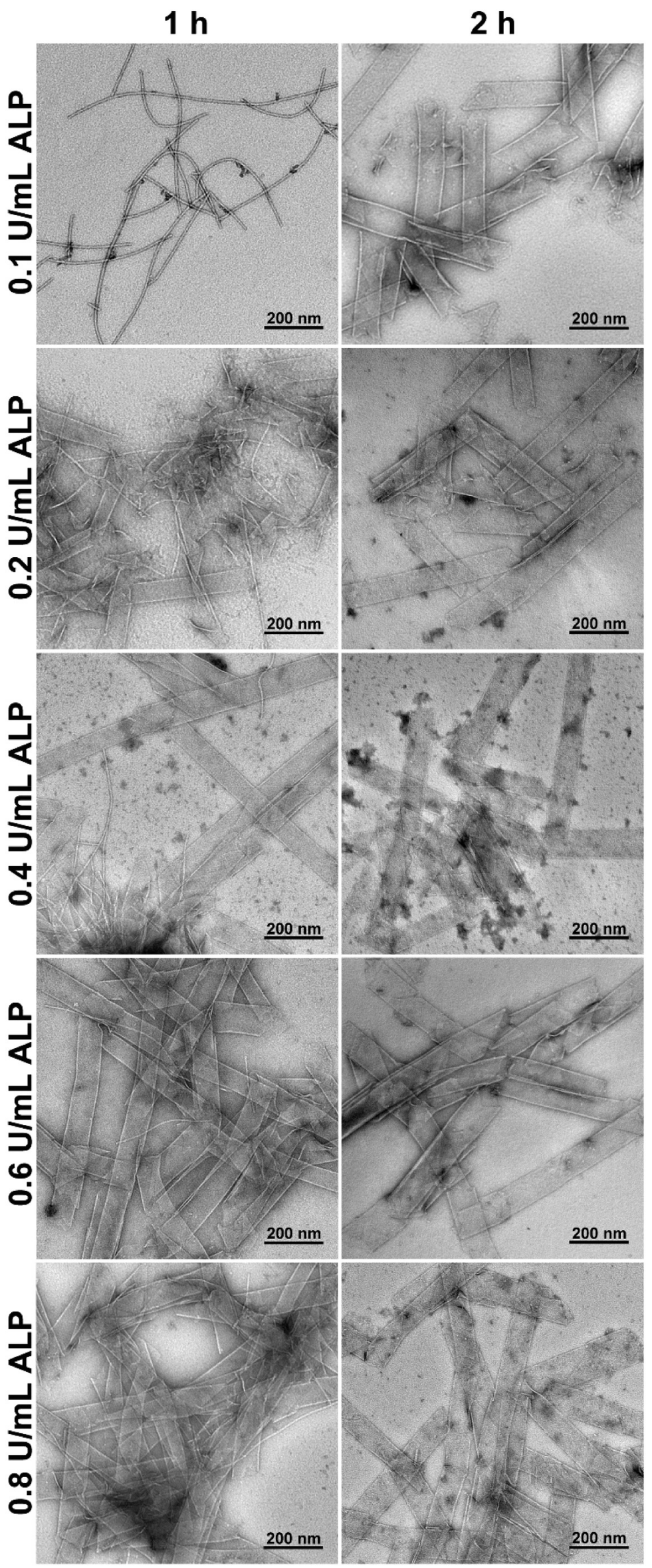

Figure 4. Transmission electron microscopy (TEM) imaging of **5** (400 μM, PBS) after dephosphorylation by ALP (0.1, 0.2, 0.4, 0.6, or 0.8 U/mL) for 1 or 2 h.

are 27.3, 21.6, and 30.6 min, respectively. After 5 h of incubation, 400 μM **5** results in a dephosphorylation ratio of 93.8%, indicating that the nanoribbons, formed after 24 h of incubation of **5** with ALP (Figure 3, top row, right), mainly consist of **6**. Decreasing the ALP concentration to 0.1 U/mL,

https://doi.org/10.1021/jacs.1c07923
J. Am. Chem. Soc. 2021, 143, 15852−15862

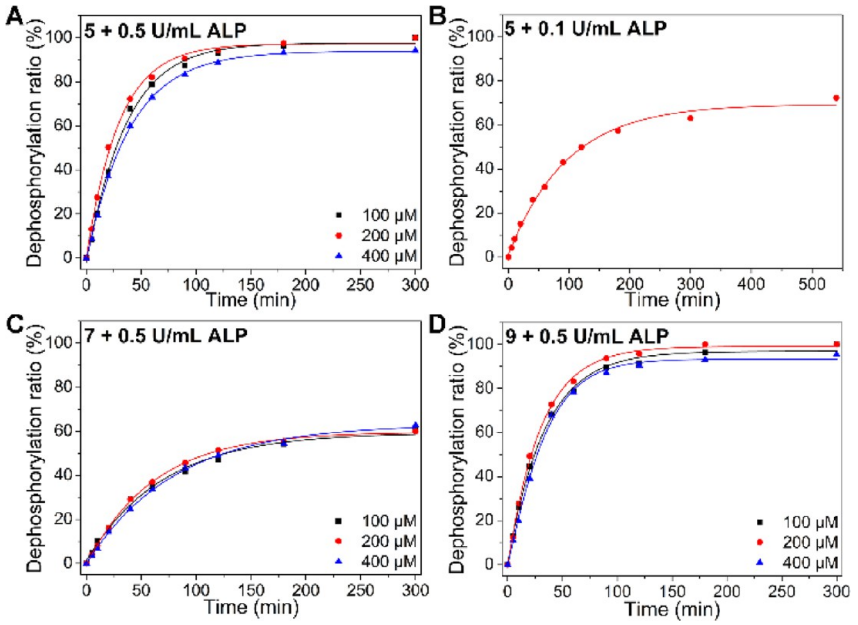

Figure 5. Time-dependent dephosphorylation of **5** by (A) ALP (0.5 U/mL) and (B) ALP (0.1 U/mL). Time-dependent dephosphorylation of (C) **7** and (D) **9** by ALP (0.5 U/mL).

the half-life of **5** (400 μM) is 122.2 min, and the final dephosphorylation ratio is 69.1% (Figure 5B). After 1 h of incubation, 32.7% of **5** turns into **6**, and long nanofibers were observed (Figure 4, first row, left). After 2 h of incubation of **5** with 0.1 U/mL ALP, 49.6% of **5** becomes **6**, and TEM shows dominantly nanoribbons (Figure 4, first row, right).

Being incubated with 0.5 U/mL ALP, **7** has a slower dephosphorylation rate than that of **5**, and the half-lives are 127.0, 112.0, and 125.5 min at 100, 200, and 400 μM, respectively (Figure 5C). After 5 h of incubation, the conversion ratio of **7** to **8** is 61.5%, which results in nanofibers (Figure 3, middle row, right). These results indicate that the phosphotyrosine in the middle of the phosphopentapeptide slows down the dephosphorylation catalyzed by ALP. Moreover, the assemblies of **7** likely hamper the interaction of phosphotyrosine with ALP. Having D-leucine as the backbone and L-phosphotyrosine at the C-terminal of the pentapeptide, **9** exhibits a similar dephosphorylation rate as that of **5**, with the half-lives of 24.6, 21.6, and 27.0 min at 100, 200, and 400 μM, respectively (Figure 5D). After 5 h of incubation, the conversion ratio of **9** to **10** is 93.3%, which results in nanofibers (Figure 3, bottom right). These results and TEM in Figure 3 suggest that the sequence of the pentapeptides also controls the morphology of nanostructures after the enzymatic reaction approaches completion.

Circular Dichroism. To understand the secondary structures of the L-phosphopentapeptide (**5**) in the assemblies without dephosphorylation and L-pentapeptide (**6**, NBD-LLLLY) in the assemblies formed by the dephosphorylation of **5**, we measure the circular dichroism (CD) spectra of **5** at different concentrations before and after the addition of ALP. The CD spectra of **5** at the concentrations ranging from 100 to 800 μM show a slight negative trough at 225−250 nm (Figure 6A, inset), which may be caused by discrete electronic transition[67] or a small amount of helix.[68] The CD band is weak because the phosphate group increases the solubility of **5**, thus disfavoring the formation of extensive peptide assemblies that would enhance the CD signals. After the addition of ALP

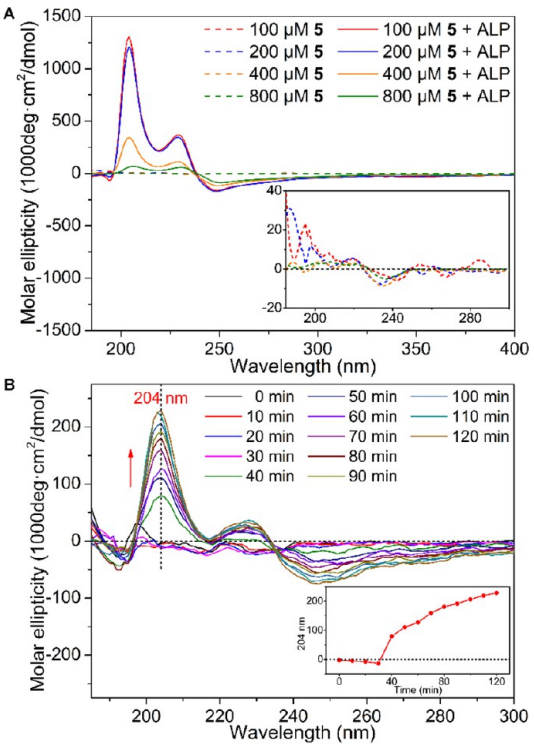

Figure 6. (A) Circular dichroism (CD) spectra of **5** (PBS) before and after dephosphorylation by 0.5 U/mL ALP for 24 h (inset: magnified CD from 190 to 300 nm). (B) The time-dependent CD spectrum of **5** (100 μM, PBS) being treated with 0.1 U/mL ALP (inset: the molar ellipticity at 204 nm).

(0.5 U/mL) in the solution of **5**, dephosphorylation of **5** produces **6**, which exhibits two positive CD bands at 204 and 229 nm, indicating the presence of α-helical conformation. The molar CD intensity of the two CD bands starts to decrease when the concentration is higher than 400 μM, agreeing with the observation that **6**, at high concentrations, aggregates to

https://doi.org/10.1021/jacs.1c07923
J. Am. Chem. Soc. 2021, 143, 15852−15862

form precipitates. For further understanding the conformation of **6**, we dissolve **6** in the mixture of trifluoroethanol (TFE) and PBS (TFE/PBS = 1/1, pH 7.4), because TFE stabilizes secondary structures.[69] The CD spectra show a positive peak at 199 nm and two negative peaks at 217 and 233 nm (Figure S17), which is the classical CD spectrum of the α-helix. Since TFE favors the formation of α-helical conformation, we decide to further examine the conformation of **5** and **6** by infrared spectroscopy. The Fourier-transform infrared (FTIR) spectra of 20 mM **5** and **6** (Figure S19) show the peak near 1453 cm^{-1} in the amide A/amide III region, which is caused by N−H stretch modes. In the amide I range, the peak at 1655 cm^{-1} is consistent with the α-helical conformation, and the peaks around 1606 and 1619 cm^{-1} likely originate from aggregated strands.[70] An additional peak at 1672 cm^{-1} is mainly due to TFA counterions bound to the peptide.[71] Although a pentapeptide is too short to observe a persistent secondary structure, the dimer of **6** (Figure 1) would be a ten-peptide sequence to allow the observation of an α-helix component. We incubate **5** (100 μM) with ALP (0.1 U/mL) and measure the CD spectra every 10 min (Figure 6B). The CD bands at 204 and 229 nm appear after a 40 min incubation (Figure 6B, inset). At the time point of 40 min, about 24% of **5** is hydrolyzed by ALP (Figure 5B). This result indicates that the morphological switch (from the micelle to nanoribbon) or significant self-assembly occurs when the ratio of [**6**] and [**5**] is about 1/3 ([**5**] = 75 μM and [**6**] = 25 μM). Notably, although NBD exhibits an absorption band in its UV−vis spectra (Figure S16) at about 344 nm, there is little induced circular dichroism (ICD) at that position. This result suggests that the dipoles of NBD moieties arrange in an antiparallel direction in the nanoribbons formed by **6** (Figure 1).

Figure 7A shows the CD spectra of **7**, and the negative band at 202 nm indicates an unordered structure.[72] The dephosphorylated product (**8**, NBD-LLYLL) shows significant different CD troughs at different concentrations. When the concentration is 100 or 200 μM, we observe a negative band around 220−250 nm. When the concentration increases to 400 and 800 μM, the negative peak blue-shifts to 212 nm. Although the ICD bands (300−350 nm) from NBD hardly show any constant trends, the presence of the ICD band from NBD indicates that NBD moieties no longer orient in a manner to reduce dipole moments. Moreover, the CD signals of **8** are significantly lower than those of **6**, suggesting the insertion of L-tyrosine between the two L-dileucines apparently weakens the ability of self-assembly of **8**. This observation agrees with that **8** only forms thin nanofibers, not nanoribbons.

As shown in Figure 7B, the CD spectra of **9** at the concentration ranging from 100 μM to 800 μM show two positive bands at 201 nm and around 223 nm, respectively, which likely originates from an unordered structure.[72] After the dephosphorylation of **9** to generate **10** (NBD-llllY), a negative band at 203 nm and positive bands around 220 nm and at 317 nm emerge. The negative band at 203 nm and positive band at 220 nm indicate the distorted α-helical conformation. The ICD bands from NBD appear at 317 nm, suggesting that NBD moieties arrange in a similar manner in the peptide assemblies of **10** formed at different concentrations. The CD signals of **10** also are weaker than those of **6**, indicating that heterochirality disfavors self-assembly of **10**. This observation also agrees with that **10** only forms thin nanofibers.

Selectively Killing iPSCs. We incubate **5**, **7**, or **9** with iPSCs and count the cells after trypan blue staining. Incubation

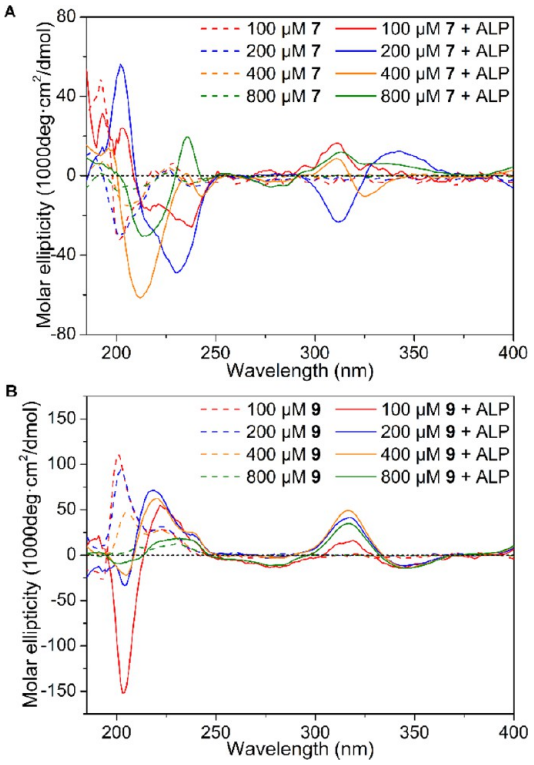

Figure 7. Circular dichroism (CD) spectra of (A) **7** and (B) **9** (PBS) before and after dephosphorylation by 0.5 U/mL ALP for 24 h.

of **5** at the concentrations of 200, 300, and 400 μM with iPSCs[73] for 2 h results in the cell viabilities of 31.05 ± 3.20%, 18.50 ± 1.50%, and 6.96 ± 1.71%, respectively, confirming that **5** potently kills iPSCs (Figure 8A and Table S1). Such an

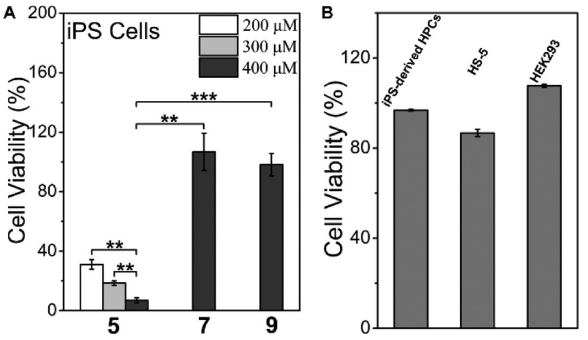

Figure 8. (A) Cell viability of iPSCs after incubating with **5**, **7**, or **9** for 2 h, ** $p < 0.01$, *** $p < 0.001$. (B) Cell viability of iPS-derived HPCs, HS-5 cells, and HEK293 cells after incubating with 400 μM **5** for 2 h.

activity is sufficient to prevent teratoma formation by iPSCs.[53] Unlike **5**, the other two phosphopentapeptides, **7** and **9**, hardly exhibit cytotoxicity against the iPSCs at 400 μM (Figure 8A and Table S2). The difference of the cytotoxicity coincides with the significant different morphologies of the assemblies of **6**, **8**, and **10** formed by enzymatic dephosphorylation but correlates less with the rates of enzymatic dephosphorylation of the phosphopeptides. This observation suggests that rapid formation of the nanoribbons made of **6** is critical for killing iPSCs. To evaluate the cell selectivity of **5**, we also test the cytotoxicity of **5** against normal cells by incubating **5** with HS-5 (bone marrow stromal cell) and HEK293 (embryonic kidney

https://doi.org/10.1021/jacs.1c07923
J. Am. Chem. Soc. 2021, 143, 15852−15862

cell).[74,75] As shown in Figure 8B, **5**, at 400 μM, exhibits slight cytotoxicity toward HS-5 cells, likely due to the high expression of acid phosphatase inside HS-5.[74] At 400 μM, **5** is innocuous to HEK293 cells (Figure 8B). The low-level expression of ALP in HS-5 or HEK293 cells also indicates that the selectivity of **5** toward iPSCs mainly originates from the levels of ALP expression. We next test the cytotoxicity of **5** against iPS-derived HPCs. After 9−10 days' differentiation, we collect the HPCs released from iPSC spheroids and analyze the hematopoietic lineage specific marker expression of harvested HPCs by flow cytometry. About 97.6% of these HPCs were CD31+ CD43+ double positive (Figure S20), indicating that HPCs have high purity. After being incubated by **5** (400 μM) for 2 h, the viability of the HPC cells is 96.8% (Figure 8B). Moreover, significant morphology change (e.g., nuclei becoming much darker) of iPSCs occurs after treatment by **5** (400 μM, 2 h, Figure S21), but there is no significant morphology change on iPS-derived HPCs after the same treatment (Figure S22). In addition, considering the inherent heterogeneity of the iPSCs or the inherent heterogeneity of the HPCs obtained from differentiation, the efficacy of **5** in Figure 8, in fact, confirms the efficiency and selectivity of **5** for eliminating iPSCs. That is, Figure 8A shows 93% cell death, agreeing with that the iPSCs generated from A21 are about 94% iPSCs in the total cell population (Figure S23). On the other hand, Figure 8B shows 97% cell survival, agreeing with that the HPCs derived from iPSCs contain about 98% HPCs and 2% iPSCs in the total cell population (Figure S20). Thus, the percentages of cell killing (Figure 8A) and cell survival (Figure 8B) are consistent with the purity of iPSCs and HPCs in the total cell population. These results indicate that **5**, by rapidly forming nanoribbons upon the dephosphorylation catalyzed by ALP, efficiently and selectively eliminates iPSCs in the mixed cell population made of iPSCs and non-iPSCs.

Intranuclear Assemblies. Because the fluorescence of NBD increases drastically from an unassembled to assembled state, we are able to use confocal laser scanning microscopy (CLSM) to reveal the cellular location of the peptide assemblies formed after dephosphorylation catalyzed by ALP. After incubation with **5** at 400 μM for 2 h, the iPSCs exhibit strong NBD fluorescence in nuclei and much weaker fluorescence in cytoplasm and on the membrane except for a few puncta (Figure 9). Moreover, the bright field image shows

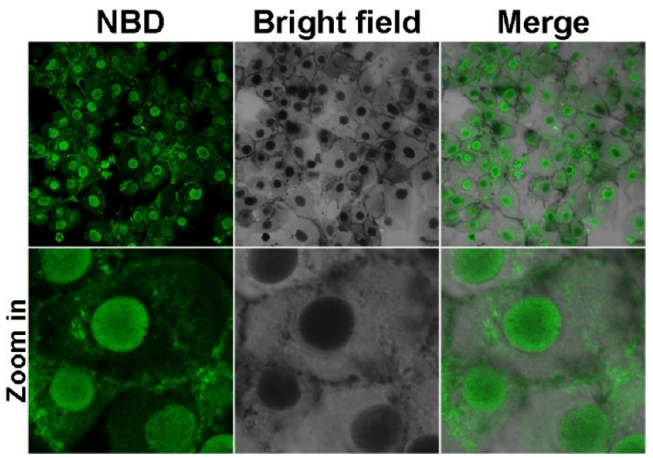

Figure 9. Confocal laser scanning microscopy (CLSM) images of iPS cells after being treated by **5** (400 μM) for 2 h.

black nuclei, as observed by an optical microscope (Figures 9 and S21). The blackness in nuclei overlaps well with the strong fluorescence. In addition, even stronger fluorescence and blackness exhibit in nucleoli (Figures 10 and S26), indicating

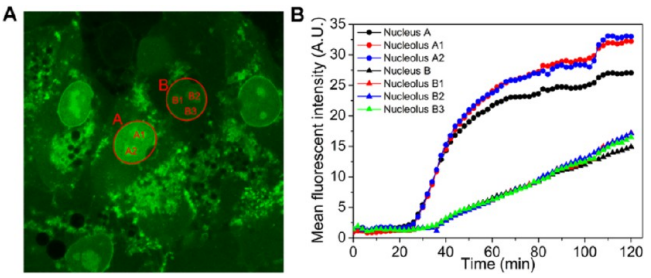

Figure 10. (A) The final fluorescent image of time-dependent CLSM of iPS cells treated by **5** (400 μM). (B) The increase of mean fluorescent intensity of the areas in (A).

that the EISA of **5** targets and aggregates in iPSC nuclei, especially in nucleoli. To understand how dephosphorylation affects nucleus-targeting, we incubate iPSCs with **5** (400 μM) and an inhibitor (2,5-dimethoxy-*N*-(quinolin-3-yl)-benzenesulfonamide (DQB), 5 μM) of tissue nonspecific alkaline phosphatase for 2 h and examine the cells by CLSM, which shows little fluorescence in cells (Figure S24). The results confirm that the nucleus-targeting mainly originates from the ALP-catalyzed dephosphorylation. The nucleus-targeting is also related to the concentration of **5**; with decreasing the concentration to 200 μM, there is hardly any fluorescence in the cells (Figure S25). This result indicates that self-assembly to form micelles/nanoparticles of **5** is crucial for the nuclear-targeting. Decreasing the treatment time to 1 h leads to weaker fluorescence and light blackness in the nuclei (Figure S26) in fluorescent and optical modes, respectively. Nevertheless, the nuclei still exhibit strong fluorescence, confirming nuclear accumulation of **6**. We also incubate iPSCs with **7** or **9** at 400 μM for 2 h. The incubation by **7** for 2 h leads to no fluorescence inside the cells (Figure S24). As to the iPSCs treated by **9** for 2 h, most of the cells exhibit no fluorescence inside the cells, several of them show NBD fluorescence on the membrane, and a few of them exhibit fluorescent puncta in the nuclei (Figure S24), which indicates a slight inhomogeneity of the iPSC populations in terms of the expression level of ALP.

To trace the dynamics of the formation and distribution of **5** inside iPS cells, we use time-lapse CLSM to image the changes of the fluorescence in the iPSCs incubated by **5** (400 μM) (Figure S27 and video 1). We pick one cell as a representative case (Figure S28, in the red dashed square) for analysis. After a 6 min incubation, fluorescent puncta appear on the membrane (as pointed to by a yellow arrow), likely originating from the aggregates of assemblies of **5** and those of **6** generated by the dephosphorylation catalyzed by ALP. This observation indicates that, as a surfactant-like peptide,[76] the assemblies of **5** first adheres to the cell membrane and then is hydrolyzed by ALP to form **6**. After a 24 min incubation, fluorescence starts to grow in the cytoplasm. Considering the LLLLY motif constitutes the transmembrane domains of 18 human membrane proteins (Table S3), we speculate that the affinity of **5** or **6** to the membrane allows the assemblies of the mixture of **5** and **6** to interact with cellular membranes for facilitating nuclear localization. At about 28 min of incubation,

https://doi.org/10.1021/jacs.1c07923
J. Am. Chem. Soc. 2021, 143, 15852−15862

fluorescence appears in the nucleus. Moreover, the nuclei shrink after the assemblies emerge in the nuclei. In addition, the nuclei also show nuclear blebbing.[77] The shrinkage of nuclei and nuclear blebbing likely associate with iPSC death (Figure S27). To further examine the dynamics of EISA-formed peptide assemblies in iPSCs at different times, we monitor the increase of fluorescence in two cells, whose nuclei are A and B (Figure 10A), respectively, over 2 h. Figure 10B shows the mean fluorescence intensity in the two nuclei and their nucleoli. The mean fluorescent intensity in Nucleus A starts to increase at 28 min and levels off after 110 min. As for Nucleus B, the mean fluorescent intensity keeps increasing from 38 min. The increases of the fluorescence in the nuclei and nucleoli are synchronous. These results suggest that the assemblies made of **5** and **6** first self-assemble on the membrane after ALP dephosphorylation to form fluorescent puncta, and then the assemblies enter the cells and quickly enter nuclei. The assemblies inside the nuclei or near nuclear membrane induce the nuclear blebbing and the shrinkage of nuclei, which likely contributes to the cell death.

Degradation of the L-Pentapeptide. As an L-peptide, **5** should be proteolytically susceptible to proteases, especially after it is converted to **6**. Thus, we test the stability of **5** in the lysate of HS-5. We prepare cell lysate from 5 million HS-5 cells resuspended in 1 mL and then incubate it with 200 μM of **5**. All of **5** disappears (transform to **6**), and only about 20% of **6** remains after 2 h of incubation. After a 4 h incubation, only 6.01% of **6** remains (Figure S29). This result agrees with that **5** hardly inhibits HS-5 cells and confirms that (i) **5** or **6**, as an L-peptide, is susceptible to proteolysis, and (ii) because it can be proteolytically hydrolyzed, **5**, after killing iPSCs, likely would lead to less side effects than D-peptides (e.g., **2**) to differentiated cells in the cell mixtures.

CONCLUSION

In summary, we report an L-leucine-rich phosphopentapeptide (**5**) that rapidly and selectively kills iPSCs by generation of intranuclear peptide assemblies via ALP-catalyzed enzymatic self-assembly. Because the morphological change of the peptide assemblies is controlled by the level of ALP and concentration of the precursors, EISA of **5** is able to control cell fates according to both levels of enzyme expression and precursor concentrations. Unlike molecules that localize in nuclei by positive charge,[78] the L-leucine-rich phosphopeptide bears negative charges. Although the exact pathway for **5** entering the nuclei of iPSCs remains to be elucidated, we speculate that the assemblies of **5** likely cluster ALP on the cell surface to facilitate cellular uptake. Then, further dephosphorylation by ALP leads to their endosomal escape before entering the nuclei of iPSCs. Such an unconventional mode of cellular uptake of phosphopeptide assemblies is recently demonstrated by overexpressing ALP on HEK293 cells.[79] Moreover, the shrinkage of nuclei and nuclear blebbing suggest that the rapid formation of nuclear assemblies of **6** may generate local oncotic pressure to contribute to the iPSC death. In addition, we speculate that the nuclear accumulation of **6**, without involving canonical nuclear location sequences,[80] implies a possible new mechanism for nucleocytoplamic transport. The results from the control compounds (**7** and **9**) indicate that both the rate of the enzymatic reaction and the molecule structures (e.g., sequence and stereochemistry) control the morphology of the resulting peptide assemblies. Although the effect of **5** on function of normal cells and iPSC-derived cells remains to be determined, the rapid degradation of **5** or **6** as unassembled L-peptide by HS-5 cells (Figure S29) suggests that the long-term effects of the **5** or **6** likely would be minimal. While EISA has frequently resulted in the peptide assemblies made of β-sheets, the exploration of α-helical peptides for EISA received less attention. This work illustrates the potential of enzymatic noncovalent synthesis for generating peptide assemblies of α-helices because a considerable amount of studies has already established a useful pool of peptides for generating helical assemblies of peptides[71,81,82] and there is rich information on the transmembrane domains of proteins.

ASSOCIATED CONTENT

Supporting Information

The Supporting Information is available free of charge at https://pubs.acs.org/doi/10.1021/jacs.1c07923.

Materials and detailed experimental procedures, figures of ^{1}H NMR, mass, UV, CD, and FTIR spectra, TEM and CLSM images, CMC, HT voltages of CD spectra, CD31, CD43, and OCT4 expression, optical photos and images, and remaining percentages of **5** and **6**, and tables of iPSC numbers and LLLLY motif (PDF)

5 (400 μM) incubates with iPSCs (2 h) (AVI)

AUTHOR INFORMATION

Corresponding Author

Bing Xu − *Department of Chemistry, Brandeis University, Waltham, Massachusetts 02454, United States;* orcid.org/0000-0002-4639-387X; Email: bxu@brandeis.edu

Authors

Shuang Liu − *Department of Chemistry, Brandeis University, Waltham, Massachusetts 02454, United States; School of Materials Science and Engineering, Wuhan University of Technology, Wuhan, Hubei 430070, China;* orcid.org/0000-0001-5548-8494

Qiuxin Zhang − *Department of Chemistry, Brandeis University, Waltham, Massachusetts 02454, United States*

Adrianna N. Shy − *Department of Chemistry, Brandeis University, Waltham, Massachusetts 02454, United States*

Meihui Yi − *Department of Chemistry, Brandeis University, Waltham, Massachusetts 02454, United States*

Hongjian He − *Department of Chemistry, Brandeis University, Waltham, Massachusetts 02454, United States*

Shijiang Lu − *HebeCell, Natick, Massachusetts 01760, United States*

Complete contact information is available at: https://pubs.acs.org/10.1021/jacs.1c07923

Funding

This work was partially supported by the NIH (CA142746) and NSF (DMR-2011846). S.L. is grateful for a scholarship from the China Scholarship Council (201906955058).

Notes

The authors declare no competing financial interest.

REFERENCES

(1) Takahashi, K.; Tanabe, K.; Ohnuki, M.; Narita, M.; Ichisaka, T.; Tomoda, K.; Yamanaka, S. Induction of Pluripotent Stem Cells from Adult Human Fibroblasts by Defined Factors. *Cell* **2007**, *131* (5), 861−872.

(2) Kriks, S.; Shim, J. W.; Piao, J.; Ganat, Y. M.; Wakeman, D. R.; Xie, Z.; Carrillo-Reid, L.; Auyeung, G.; Antonacci, C.; Buch, A.; Yang, L.; Beal, M. F.; Surmeier, D. J.; Kordower, J. H.; Tabar, V.; Studer, L. Dopamine neurons derived from human ES cells efficiently engraft in animal models of Parkinson's disease. *Nature* **2011**, *480* (7378), 547−51.
(3) Zhang, J.; Wilson, G. F.; Soerens, A. G.; Koonce, C. H.; Yu, J.; Palecek, S. P.; Thomson, J. A.; Kamp, T. J. Functional cardiomyocytes derived from human induced pluripotent stem cells. *Circ. Res.* **2009**, *104* (4), e30−e41.
(4) Witty, A. D.; Mihic, A.; Tam, R. Y.; Fisher, S. A.; Mikryukov, A.; Shoichet, M. S.; Li, R. K.; Kattman, S. J.; Keller, G. Generation of the epicardial lineage from human pluripotent stem cells. *Nat. Biotechnol.* **2014**, *32* (10), 1026−35.
(5) Pagliuca, F. W.; Millman, J. R.; Gurtler, M.; Segel, M.; Van Dervort, A.; Ryu, J. H.; Peterson, Q. P.; Greiner, D.; Melton, D. A. Generation of functional human pancreatic beta cells in vitro. *Cell* **2014**, *159* (2), 428−39.
(6) Barnea-Cramer, A. O.; Wang, W.; Lu, S. J.; Singh, M. S.; Luo, C.; Huo, H.; McClements, M. E.; Barnard, A. R.; MacLaren, R. E.; Lanza, R. Function of human pluripotent stem cell-derived photoreceptor progenitors in blind mice. *Sci. Rep.* **2016**, *6*, 29784.
(7) Sharma, R.; Khristov, V.; Rising, A.; Jha, B. S.; Dejene, R.; Hotaling, N.; Li, Y.; Stoddard, J.; Stankewicz, C.; Wan, Q.; Zhang, C.; Campos, M. M.; Miyagishima, K. J.; McGaughey, D.; Villasmil, R.; Mattapallil, M.; Stanzel, B.; Qian, H.; Wong, W.; Chase, L.; Charles, S.; McGill, T.; Miller, S.; Maminishkis, A.; Amaral, J.; Bharti, K. Clinical-grade stem cell-derived retinal pigment epithelium patch rescues retinal degeneration in rodents and pigs. *Sci. Transl. Med.* **2019**, *11* (475), eaat5580.
(8) Yamanaka, S. Pluripotent Stem Cell-Based Cell Therapy—Promise and Challenges. *Cell Stem Cell* **2020**, *27* (4), 523−531.
(9) Harding, J.; Mirochnitchenko, O. Preclinical studies for induced pluripotent stem cell-based therapeutics. *J. Biol. Chem.* **2014**, *289* (8), 4585−4593.
(10) Knoepfler, P. S. Deconstructing stem cell tumorigenicity: A roadmap to safe regenerative medicine. *Stem Cells* **2009**, *27* (5), 1050−1056.
(11) Kanemura, H.; Go, M. J.; Shikamura, M.; Nishishita, N.; Sakai, N.; Kamao, H.; Mandai, M.; Morinaga, C.; Takahashi, M.; Kawamata, S. Tumorigenicity studies of induced pluripotent stem cell (iPSC)-derived retinal pigment epithelium (RPE) for the treatment of age-related macular degeneration. *PLoS One* **2014**, *9* (1), e85336.
(12) Kawamata, S.; Kanemura, H.; Sakai, N.; Takahashi, M.; Go, M. J. Design of a Tumorigenicity Test for Induced Pluripotent Stem Cell (iPSC)-Derived Cell Products. *J. Clin. Med.* **2015**, *4* (1), 159−71.
(13) Liu, Z.; Tang, Y.; Lu, S.; Zhou, J.; Du, Z.; Duan, C.; Li, Z.; Wang, C. The tumourigenicity of iPS cells and their differentiated derivates. *J. Cell. Mol. Med.* **2013**, *17* (6), 782−91.
(14) Hu, B. Y.; Weick, J. P.; Yu, J.; Ma, L. X.; Zhang, X. Q.; Thomson, J. A.; Zhang, S. C. Neural differentiation of human induced pluripotent stem cells follows developmental principles but with variable potency. *Proc. Natl. Acad. Sci. U. S. A.* **2010**, *107* (9), 4335−40.
(15) Schuldiner, M.; Itskovitz-Eldor, J.; Benvenisty, N. Selective ablation of human embryonic stem cells expressing a "suicide" gene. *Stem Cells* **2003**, *21* (3), 257−265.
(16) Choo, A. B.; Heng, L. T.; Sheu, N. A.; Wey, J. F.; Chin, A.; Lo, J.; Zheng, L.; Hentze, H.; Philp, R. J.; Oh, S. K. W.; Yap, M. Selection against undifferentiated human embryonic stem cells by a cytotoxic antibody recognizing podocalyxin-like protein-1. *Stem Cells* **2008**, *26* (6), 1454−1463.
(17) Tateno, H.; Onuma, Y.; Ito, Y.; Minoshima, F.; Saito, S.; Shimizu, M.; Aiki, Y.; Asashima, M.; Hirabayashi, J. Elimination of tumorigenic human pluripotent stem cells by a recombinant lectin-toxin fusion protein. *Stem Cell Rep.* **2015**, *4* (5), 811−820.
(18) Tateno, H. Development of lectin-drug conjugates for elimination of undifferentiated cells and cancer therapy. *Trends Glycosci. Glycotechnol.* **2019**, *31* (183), E121−E127.
(19) Fong, C. Y.; Peh, G. S. L.; Gauthaman, K.; Bongso, A. Separation of SSEA-4 and TRA-1−60 labelled undifferentiated human embryonic stem cells from a heterogeneous cell population using magnetic-activated cell sorting (MACS) and fluorescence-activated cell sorting (FACS). *Stem Cell Rev.* **2009**, *5* (1), 72−80.
(20) Menendez, S.; Camus, S.; Herreria, A.; Paramonov, I.; Morera, L. B.; Collado, M.; Pekarik, V.; Maceda, I.; Edel, M.; Consiglio, A.; Sanchez, A.; Li, H.; Serrano, M.; Belmonte, J. C. I. Increased dosage of tumor suppressors limits the tumorigenicity of iPS cells without affecting their pluripotency. *Aging Cell* **2012**, *11* (1), 41−50.
(21) Miki, K.; Endo, K.; Takahashi, S.; Funakoshi, S.; Takei, I.; Katayama, S.; Toyoda, T.; Kotaka, M.; Takaki, T.; Umeda, M.; Okubo, C.; Nishikawa, M.; Oishi, A.; Narita, M.; Miyashita, I.; Asano, K.; Hayashi, K.; Osafune, K.; Yamanaka, S.; Saito, H.; Yoshida, Y. Efficient Detection and Purification of Cell Populations Using Synthetic MicroRNA Switches. *Cell Stem Cell* **2015**, *16* (6), 699−711.
(22) Matsumoto, R.; Shimizu, K.; Nagashima, T.; Tanaka, H.; Mizuno, M.; Kikkawa, F.; Hori, M.; Honda, H. Plasma-activated medium selectively eliminates undifferentiated human induced pluripotent stem cells. *Regen. Ther.* **2016**, *5*, 55−63.
(23) Okada, M.; Tada, Y.; Seki, T.; Tohyama, S.; Fujita, J.; Suzuki, T.; Shimomura, M.; Ofuji, K.; Kishino, Y.; Nakajima, K.; Tanosaki, S.; Someya, S.; Kanazawa, H.; Senju, S.; Nakatsura, T.; Fukuda, K. Selective elimination of undifferentiated human pluripotent stem cells using pluripotent state-specific immunogenic antigen Glypican-3. *Biochem. Biophys. Res. Commun.* **2019**, *511* (3), 711−717.
(24) Shiraki, N.; Shiraki, Y.; Tsuyama, T.; Obata, F.; Miura, M.; Nagae, G.; Aburatani, H.; Kume, K.; Endo, F.; Kume, S. Methionine metabolism regulates maintenance and differentiation of human pluripotent stem cells. *Cell Metab.* **2014**, *19* (5), 780−794.
(25) Nagashima, T.; Shimizu, K.; Matsumoto, R.; Honda, H. Selective Elimination of Human Induced Pluripotent Stem Cells Using Medium with High Concentration of L-Alanine. *Sci. Rep.* **2018**, *8* (1), 12427.
(26) Blum, B.; Bar-Nur, O.; Golan-Lev, T.; Benvenisty, N. The anti-apoptotic gene survivin contributes to teratoma formation by human embryonic stem cells. *Nat. Biotechnol.* **2009**, *27* (3), 281−287.
(27) Ben-David, U.; Nudel, N.; Benvenisty, N. Immunologic and chemical targeting of the tight-junction protein Claudin-6 eliminates tumorigenic human pluripotent stem cells. *Nat. Commun.* **2013**, *4*, 1992.
(28) Kuo, T. F.; Mao, D.; Hirata, N.; Khambu, B.; Kimura, Y.; Kawase, E.; Shimogawa, H.; Ojika, M.; Nakatsuji, N.; Ueda, K.; Uesugi, M. Selective elimination of human pluripotent stem cells by a marine natural product derivative. *J. Am. Chem. Soc.* **2014**, *136* (28), 9798−9801.
(29) Mao, D.; Ando, S.; Sato, S. I.; Qin, Y.; Hirata, N.; Katsuda, Y.; Kawase, E.; Kuo, T. F.; Minami, I.; Shiba, Y.; Ueda, K.; Nakatsuji, N.; Uesugi, M. A Synthetic Hybrid Molecule for the Selective Removal of Human Pluripotent Stem Cells from Cell Mixtures. *Angew. Chem., Int. Ed.* **2017**, *56* (7), 1765−1770.
(30) Mao, D.; Chung, X. K. W.; Andoh-Noda, T.; Qin, Y.; Sato, S. I.; Takemoto, Y.; Akamatsu, W.; Okano, H.; Uesugi, M. Chemical decontamination of iPS cell-derived neural cell mixtures. *Chem. Commun.* **2018**, *54* (11), 1355−1358.
(31) Go, Y. H.; Lim, C.; Jeong, H. C.; Kwon, O. S.; Chung, S.; Lee, H.; Kim, W.; Suh, Y. G.; Son, W. S.; Lee, M. O.; Cha, H. J.; Kim, S. H. Structure-activity relationship analysis of YM155 for inducing selective cell death of human pluripotent stem cells. *Front. Chem.* **2019**, *7* (APR), 298.
(32) Kim, A.; Lee, S. Y.; Seo, C. S.; Chung, S. K. Ethanol extract of Magnoliae cortex (EEMC) limits teratoma formation of pluripotent stem cells by selective elimination of undifferentiated cells through the p53-dependent mitochondrial apoptotic pathway. *Phytomedicine* **2020**, *69*, 153198.
(33) Kondo, T. Selective eradication of pluripotent stem cells by inhibiting DHODH activity. *Stem Cells* **2020**, *39* (1), 33−42.

https://doi.org/10.1021/jacs.1c07923
J. Am. Chem. Soc. 2021, 143, 15852−15862

(34) Hermann, A.; Storch, A.; Liebau, S. Possible applications of new stem cell sources in neurology. *Nervenarzt* **2013**, *84* (8), 943−948.
(35) Rampoldi, A.; Crooke, S. N.; Preininger, M. K.; Jha, R.; Maxwell, J.; Ding, L.; Spearman, P.; Finn, M. G.; Xu, C. Targeted Elimination of Tumorigenic Human Pluripotent Stem Cells Using Suicide-Inducing Virus-like Particles. *ACS Chem. Biol.* **2018**, *13* (8), 2329−2338.
(36) Hong, H.; Takahashi, K.; Ichisaka, T.; Aoi, T.; Kanagawa, O.; Nakagawa, M.; Okita, K.; Yamanaka, S. Suppression of induced pluripotent stem cell generation by the p53-p21 pathway. *Nature* **2009**, *460* (7259), 1132−1135.
(37) Stefkova, K.; Prochazkova, J.; Pachernik, J. Alkaline phosphatase in stem cells. *Stem Cells Int.* **2015**, *2015*, 628368.
(38) Yang, Z.; Gu, H.; Fu, D.; Gao, P.; Lam, J. K.; Xu, B. Enzymatic Formation of Supramolecular Hydrogels. *Adv. Mater.* **2004**, *16* (16), 1440−1444.
(39) He, H.; Lin, X.; Wu, D.; Wang, J.; Guo, J.; Green, D. R.; Zhang, H.; Xu, B. Enzymatic Noncovalent Synthesis for Mitochondrial Genetic Engineering of Cancer Cells. *Cell Rep. Phys. Sci.* **2020**, *1* (12), 100270.
(40) Feng, Z.; Han, X.; Wang, H.; Tang, T.; Xu, B. Enzyme-Instructed Peptide Assemblies Selectively Inhibit Bone Tumors. *Chem.* **2019**, *5* (9), 2442−2449.
(41) Wang, H.; Feng, Z.; Xu, B. Intercellular Instructed-Assembly Mimics Protein Dynamics To Induce Cell Spheroids. *J. Am. Chem. Soc.* **2019**, *141* (18), 7271−7274.
(42) Yan, R.; Hu, Y.; Liu, F.; Wei, S.; Fang, D.; Shuhendler, A. J.; Liu, H.; Chen, H.; Ye, D. Activatable NIR Fluorescence/MRI Bimodal Probes for in Vivo Imaging by Enzyme-Mediated Fluorogenic Reaction and Self-Assembly. *J. Am. Chem. Soc.* **2019**, *141* (26), 10331−10341.
(43) Yang, L.; Peltier, R.; Zhang, M.; Song, D.; Huang, H.; Chen, G.; Chen, Y.; Zhou, F.; Hao, Q.; Bian, L.; He, M.; Wang, Z.; Hu, Y.; Sun, H. Desuccinylation-Triggered Peptide Self-Assembly: Live Cell Imaging of SIRT5 Activity and Mitochondrial Activity Modulation. *J. Am. Chem. Soc.* **2020**, *142* (42), 18150−18159.
(44) Cheng, D.; Wang, D.; Gao, Y.; Wang, L.; Qiao, Z.; Wang, H. Autocatalytic Morphology Transformation Platform for Targeted Drug Accumulation. *J. Am. Chem. Soc.* **2019**, *141* (10), 4406−4411.
(45) Wang, Y.; Hu, X.; Weng, J.; Li, J.; Fan, Q.; Zhang, Y.; Ye, D. A Photoacoustic Probe for the Imaging of Tumor Apoptosis by Caspase-Mediated Macrocyclization and Self-Assembly. *Angew. Chem., Int. Ed.* **2019**, *58* (15), 4886−4890.
(46) Tanaka, A.; Fukuoka, Y.; Morimoto, Y.; Honjo, T.; Koda, D.; Goto, M.; Maruyama, T. Cancer Cell Death Induced by the Intracellular Self-Assembly of an Enzyme-Responsive Supramolecular Gelator. *J. Am. Chem. Soc.* **2015**, *137* (2), 770−775.
(47) Chen, Z.; Chen, M.; Cheng, Y.; Kowada, T.; Xie, J.; Zheng, X.; Rao, J. Exploring the Condensation Reaction between Aromatic Nitriles and Amino Thiols To Optimize In Situ Nanoparticle Formation for the Imaging of Proteases and Glycosidases in Cells. *Angew. Chem., Int. Ed.* **2020**, *59* (8), 3272−3279.
(48) Shi, J.; Schneider, J. P. De novo Design of Selective Membrane-Active Peptides by Enzymatic Control of Their Conformational Bias on the Cell Surface. *Angew. Chem., Int. Ed.* **2019**, *58* (39), 13706−13710.
(49) Wang, F.; Su, H.; Xu, D.; Dai, W.; Zhang, W.; Wang, Z.; Anderson, C. F.; Zheng, M.; Oh, R.; Wan, F.; Cui, H. Tumour sensitization via the extended intratumoural release of a STING agonist and camptothecin from a self-assembled hydrogel. *Nat. Biomed. Eng.* **2020**, *4* (11), 1090−1101.
(50) Yang, Z. M.; Xu, K. M.; Guo, Z. F.; Guo, Z. H.; Xu, B. Intracellular Enzymatic Formation of Nanofibers Results in Hydrogelation and Regulated Cell Death. *Adv. Mater.* **2007**, *19* (20), 3152−3156.
(51) Kuang, Y.; Shi, J.; Li, J.; Yuan, D.; Alberti, K. A.; Xu, Q.; Xu, B. Pericellular hydrogel/nanonets inhibit cancer cells. *Angew. Chem., Int. Ed.* **2014**, *53* (31), 8104−8107.
(52) Pires, R. A.; Abul-Haija, Y. M.; Costa, D. S.; Novoa-Carballal, R.; Reis, R. L.; Ulijn, R. V.; Pashkuleva, I. Controlling Cancer Cell Fate Using Localized Biocatalytic Self-Assembly of an Aromatic Carbohydrate Amphiphile. *J. Am. Chem. Soc.* **2015**, *137* (2), 576−579.
(53) Kuang, Y.; Miki, K.; Parr, C. J. C.; Hayashi, K.; Takei, I.; Li, J.; Iwasaki, M.; Nakagawa, M.; Yoshida, Y.; Saito, H. Efficient, Selective Removal of Human Pluripotent Stem Cells via Ecto-Alkaline Phosphatase-Mediated Aggregation of Synthetic Peptides. *Cell Chem. Biol.* **2017**, *24* (6), 685−694.e4.
(54) Thul, P. J.; Akesson, L.; Wiking, M.; Mahdessian, D.; Geladaki, A.; Ait Blal, H.; Alm, T.; Asplund, A.; Bjork, L.; Breckels, L. M.; Backstrom, A.; Danielsson, F.; Fagerberg, L.; Fall, J.; Gatto, L.; Gnann, C.; Hober, S.; Hjelmare, M.; Johansson, F.; Lee, S.; Lindskog, C.; Mulder, J.; Mulvey, C. M.; Nilsson, P.; Oksvold, P.; Rockberg, J.; Schutten, R.; Schwenk, J. M.; Sivertsson, A.; Sjostedt, E.; Skogs, M.; Stadler, C.; Sullivan, D. P.; Tegel, H.; Winsnes, C.; Zhang, C.; Zwahlen, M.; Mardinoglu, A.; Ponten, F.; von Feilitzen, K.; Lilley, K. S.; Uhlen, M.; Lundberg, E. A subcellular map of the human proteome. *Science* **2017**, *356* (6340), eaal3321.
(55) Haass, C.; Selkoe, D. J. Soluble protein oligomers in neurodegeneration: lessons from the Alzheimer's amyloid beta-peptide. *Nat. Rev. Mol. Cell Biol.* **2007**, *8* (2), 101−12.
(56) Nelson, R.; Sawaya, M. R.; Balbirnie, M.; Madsen, A. O.; Riekel, C.; Grothe, R.; Eisenberg, D. Structure of the cross-beta spine of amyloid-like fibrils. *Nature* **2005**, *435* (7043), 773−8.
(57) He, H.; Tan, W.; Guo, J.; Yi, M.; Shy, A. N.; Xu, B. Enzymatic Noncovalent Synthesis. *Chem. Rev.* **2020**, *120* (18), 9994−10078.
(58) Lyu, P. C.; Sherman, J. C.; Chen, A.; Kallenbach, N. R. Alpha-helix stabilization by natural and unnatural amino acids with alkyl side chains. *Proc. Natl. Acad. Sci. U. S. A.* **1991**, *88* (12), 5317−5320.
(59) Feng, Z.; Wang, H.; Wang, F.; Oh, Y.; Berciu, C.; Cui, Q.; Egelman, E. H.; Xu, B. Artificial Intracellular Filaments. *Cell Rep. Phys. Sci.* **2020**, *1* (7), 100085.
(60) Gao, Y.; Shi, J.; Yuan, D.; Xu, B. Imaging enzyme-triggered self-assembly of small molecules inside live cells. *Nat. Commun.* **2012**, *3*, 1033.
(61) Nick Pace, C.; Martin Scholtz, J. A Helix Propensity Scale Based on Experimental Studies of Peptides and Proteins. *Biophys. J.* **1998**, *75* (1), 422−427.
(62) Cai, Y.; Shi, Y.; Wang, H.; Wang, J.; Ding, D.; Wang, L.; Yang, Z. Environment-Sensitive Fluorescent Supramolecular Nanofibers for Imaging Applications. *Anal. Chem.* **2014**, *86* (4), 2193−2199.
(63) Burtis, C. A.; Ashwood, E. R.; Bruns, D. E. *Tietz Textbook of Clinical Chemistry and Molecular Diagnostics*; Elsevier Saunders: MO, 2006.
(64) Abdallah, E. A. A.; Said, R. N.; Mosallam, D. S.; Moawad, E. M. I.; Kamal, N. M.; Fathallah, M. G. E. Serial serum alkaline phosphatase as an early biomarker for osteopenia of prematurity. *Medicine (Philadelphia, PA, U. S.)* **2016**, *95* (37), e4837.
(65) Gibson, C. J.; Britton, K. A.; Miller, A. L.; Loscalzo, J. Clinical problem-solving. Out of the blue. *N. Engl. J. Med.* **2014**, *370* (18), 1742−8.
(66) Guo, J.; He, H.; Kim, B. J.; Wang, J.; Yi, M.; Lin, C.; Xu, B. The ratio of hydrogelator to precursor controls the enzymatic hydrogelation of a branched peptide. *Soft Matter* **2020**, *16* (44), 10101−10105.
(67) Rippon, W. B.; Hiltner, W. A. The 225−240-nm Circular Dichroism Band in Disordered and Charged Polypeptides. *Macromolecules* **1973**, *6* (2), 282−285.
(68) Myer, Y. P. The pH-Induced Helix-Coil Transition of Poly-L-lysine and Poly-L-glutamic Acid and the 238-mμ Dichroic Band. *Macromolecules* **1969**, *2* (6), 624−628.
(69) Roccatano, D.; Colombo, G.; Fioroni, M.; Mark, A. E. Mechanism by which 2,2,2-trifluoroethanol/water mixtures stabilize secondary-structure formation in peptides: A molecular dynamics study. *Proc. Natl. Acad. Sci. U. S. A.* **2002**, *99* (19), 12179−12184.
(70) bagińska, K.; Makowska, J.; Wiczk, W.; Kasprzykowski, F.; ChmurzyńSKI, L. Conformational studies of alanine-rich peptide using CD and FTIR spectroscopy. *J. Pept. Sci.* **2008**, *14* (3), 283−289.

https://doi.org/10.1021/jacs.1c07923
J. Am. Chem. Soc. 2021, 143, 15852−15862

(71) Castelletto, V.; Seitsonen, J.; Ruokolainen, J.; Hamley, I. W. Alpha helical surfactant-like peptides self-assemble into pH-dependent nanostructures. *Soft Matter* **2021**, *17* (11), 3096−3104.
(72) Gekko, K.; Matsuo, K. Vacuum-ultraviolet circular dichroism analysis of biomolecules. *Chirality* **2006**, *18* (5), 329−334.
(73) Takahashi, K.; Yamanaka, S. Induction of Pluripotent Stem Cells from Mouse Embryonic and Adult Fibroblast Cultures by Defined Factors. *Cell* **2006**, *126* (4), 663−676.
(74) Roecklein, B. A.; Torok-Storb, B. Functionally distinct human marrow stromal cell lines immortalized by transduction with the human papilloma virus E6/E7 genes. *Blood* **1995**, *85* (4), 997−1005.
(75) Su, G.; Zhao, Y.; Wei, J.; Han, J.; Chen, L.; Xiao, Z.; Chen, B.; Dai, J. The effect of forced growth of cells into 3D spheres using low attachment surfaces on the acquisition of stemness properties. *Biomaterials* **2013**, *34* (13), 3215−3222.
(76) Vauthey, S.; Santoso, S.; Gong, H.; Watson, N.; Zhang, S. Molecular self-assembly of surfactant-like peptides to form nanotubes and nanovesicles. *Proc. Natl. Acad. Sci. U. S. A.* **2002**, *99* (8), 5355−5360.
(77) Stephens, A. D.; Liu, P. Z.; Banigan, E. J.; Almassalha, L. M.; Backman, V.; Adam, S. A.; Goldman, R. D.; Marko, J. F. Chromatin histone modifications and rigidity affect nuclear morphology independent of lamins. *Mol. Biol. Cell* **2018**, *29* (2), 220−233.
(78) Cai, Y.; Shen, H.; Zhan, J.; Lin, M.; Dai, L.; Ren, C.; Shi, Y.; Liu, J.; Gao, J.; Yang, Z. Supramolecular "Trojan Horse" for Nuclear Delivery of Dual Anticancer Drugs. *J. Am. Chem. Soc.* **2017**, *139* (8), 2876−2879.
(79) He, H.; Guo, J.; Xu, J.; Wang, J.; Liu, S.; Xu, B. Dynamic Continuum of Nanoscale Peptide Assemblies Facilitates Endocytosis and Endosomal Escape. *Nano Lett.* **2021**, *21* (9), 4078−4085.
(80) Dingwall, C.; Laskey, R. A. Nuclear targeting sequences — a consensus? *Trends Biochem. Sci.* **1991**, *16*, 478−481.
(81) Rhys, G. G.; Wood, C. W.; Beesley, J. L.; Zaccai, N. R.; Burton, A. J.; Brady, R. L.; Thomson, A. R.; Woolfson, D. N. Navigating the Structural Landscape of De Novo α-Helical Bundles. *J. Am. Chem. Soc.* **2019**, *141* (22), 8787−8797.
(82) Wang, F.; Gnewou, O.; Modlin, C.; Beltran, L. C.; Xu, C.; Su, Z.; Juneja, P.; Grigoryan, G.; Egelman, E. H.; Conticello, V. P. Structural analysis of cross α-helical nanotubes provides insight into the designability of filamentous peptide nanomaterials. *Nat. Commun.* **2021**, *12* (1), 407.

https://doi.org/10.1021/jacs.1c07923
J. Am. Chem. Soc. 2021, 143, 15852−15862